FULL PAPER

Magnetic Resonance in Medicine 00:00–00 (2017)

Optimized Inversion-Time Schedules for Quantitative T_1 Measurements Based on High-Resolution Multi-Inversion EPI

Ouri Cohen[1,2]* and Jonathan R. Polimeni[1,2,3]

Purpose: Demonstrate an optimized multi-inversion echo-planar imaging technique to accelerate quantitative T_1 mapping by judicious selection of inversion times for each slice.

Methods: Slice ordering is optimized to maximize discrimination between tissues with different T_1 values. The optimized slice orderings are tested in the International Society for Magnetic Resonance in Medicine/National Institute of Standards and Technology phantom and compared with an unoptimized 21-measurement acquisition. The utility of the method is demonstrated in a healthy subject in vivo at 3 T and validated with a gold-standard inversion-recovery sequence. The in vivo precision of our technique was tested by repeated scans of the same subject within a scan session and across scan sessions, occurring 28 days apart.

Results: Phantom measurements yielded good agreement ($R^2 = 0.99$) between the T_1 estimates from the proposed optimized protocol, reference values from the National Institute of Standards and Technology phantom and gold-standard inversion-recovery values, as well as a negligible estimation bias that was slightly lower than that from the unoptimized 21-measurement protocol (0.74 versus 19 ms). The range of values for the scan–rescan coefficient of variation was 0.86 to 0.93 (within session) and 0.83 to 0.92 (across sessions) across all scan durations tested.

Conclusions: Optimized slice orderings allow faster quantitative T_1 mapping. The optimized sequence yielded accurate and precise T_1 maps. **Magn Reson Med 000:000–000, 2017.**
© 2017 International Society for Magnetic Resonance in Medicine.

Key words: EPI; MR fingerprinting; MR relaxation; T_1 mapping

INTRODUCTION

Two-dimensional inversion-recovery (IR) pulse sequences are used commonly for quantitative T_1 mapping. To estimate T_1, each image slice is acquired with multiple inversion time (TI) values, and the measured image intensities are then fitted to a model to extract the underlying quantitative T_1 recovery value at each voxel. Although reliable, this T_1 mapping procedure suffers from lengthy acquisition durations that prevent its use in routine clinical scans. To increase efficiency, rather than acquiring only one slice per IR, faster alternatives acquire multiple slices sequentially following each non-spatially selective inversion pulse such that each of the slices is acquired at different TIs (1–3). The temporal ordering of the slices is permuted from one IR period to the next, such that during the repeated inversion recoveries each slice is measured with a distinct ordering of TI values. This multiple-slice scheme provides increased signal in each measured slice relative to the Look-Locker approach (4–6), in which the same slice is excited and acquired multiple times during the IR to sample multiple TI values with the disadvantage that there is little time for signal recovery (longitudinal relaxation) in the slice between excitations. In the multiple-slice scheme, the repetition time (TR) for any given slice may vary from one IR period to the next, and in general for fast acquisitions, TR is too short for complete longitudinal recovery (in some cases, $TR < T_1$); therefore, fitting the T_1 value using a closed-form model can be challenging (7,8). Instead, the resulting image intensities for a given slice can be matched to a dictionary of signal recovery curves, precomputed using the Bloch simulation of the specific pulse sequence for a variety of possible T_1 values (9).

The image acquisition during the IR can be accomplished with different image-encoding schemes, but the echo-planar imaging (EPI) sequence offers compelling benefits. In addition to a rapid acquisition, EPI is the most commonly used acquisition technique for functional MRI (10), as well as diffusion and perfusion MRI (11), which are typically acquired alongside separate anatomical reference scans to localize regions of interest. Because EPI is vulnerable to geometric distortion as a result of its low phase-encoding bandwidth (12), the EPI data must be distortion-corrected to achieve an accurate geometric alignment to anatomical reference images obtained with standard pulse sequences such as magnetization-prepared rapid gradient echo (13,14). The limited accuracy of distortion correction has driven recent interest in EPI-based anatomical reference data using the same phase-encoding bandwidth used in the

[1]Athinoula A. Martinos Center for Biomedical Imaging, Massachusetts General Hospital, Charlestown, Massachusetts, USA.

[2]Department of Radiology, Harvard Medical School, Boston, Massachusetts, USA.

[3]Harvard-MIT Division of Health Sciences and Technology, Massachusetts Institute of Technology, Cambridge, Massachusetts, USA.

This work was supported in part by the NIH National Institute for Biomedical Imaging and Bioengineering (P41-EB015896, K01-EB011498, and R01-EB019437) and by the MGH/HST Athinoula A. Martinos Center for Biomedical Imaging, and was made possible by the resources provided by Shared Instrumentation Grants S10-RR023401, S10-RR019307, S10-RR023043, S10-RR019371, and S10-RR020948.

*Correspondence to: Ouri Cohen, Ph.D., Department of Radiology, Athinoula A. Martinos Center for Biomedical Imaging, Room 2320, Massachusetts General Hospital, 149 13th Street, Charlestown, MA 02129, USA. E-mail: ouri@nmr.mgh.harvard.edu.

Received 28 March 2017; revised 2 August 2017; accepted 4 August 2017

DOI 10.1002/mrm.26889

Published online 00 Month 2017 in Wiley Online Library (wileyonlinelibrary.com).

© 2017 International Society for Magnetic Resonance in Medicine

functional (or diffusion/perfusion) acquisition, to perfectly match the geometric distortion of the two data sets (15–20).

In previous work (9), we described a multi-inversion EPI sequence to provide a quantitative T_1 map that is distortion-matched to EPI-based functional MRI data. To ensure accurate reconstruction of the multiple different T_1 values present in the human brain, multiple measurements were acquired across multiple IR periods and the slice order permuted by a constant "skip factor" between each measurement, with the skip factor defined as the offset from a linear ordering of N slices (i.e., the number of slices permuted or "skipped" at the beginning of the IR period and acquired at the end). Unfortunately, given the broad range of T_1 values in the human brain, a large number of measurements are needed to acquire the required broad range of TI values in each slice for accurate T_1 mapping, resulting in prolonged scan time for a single volume (up to 3 min). Moreover, the choice of skip factor is arbitrary and not optimized for the anatomy of interest.

Instead, in this work we use concepts originally developed for flip angle and TR schedule optimization in MR fingerprinting (MRF) (21–25) to select the optimal slice ordering, namely, one that produces the set of distinct TI values sampled by each slice that maximizes the discrimination between different tissue types for a presumed range of tissue T_1 values. We demonstrate that this optimization allows one to reduce the required number of measurements without adversely affecting the quantitative accuracy and precision of the T_1 maps obtained. Our method is demonstrated in phantom data and in an in vivo data set from a healthy subject scanned at 3 T.

THEORY

Reconstruction Dictionary Design

We briefly review here the design of the reconstruction dictionary. The reader is referred to (9) for further details. Let $TI_{j,k}$ be the TI undergone by a slice j in measurement k in a given slice-ordering scheme. Because the acquisition time of each slice is constant, the TIs can be converted into a specific slice order by dividing by the acquisition time per slice. The evolution of the signal intensity S in each voxel within a given slice j can be modeled as a vector $\mathbf{d}(T_1)=[S(TI_{j,1}),\ S(TI_{j,2}),\ \ldots]$, in which the dependence of the signal on the tissue's underlying T_1 value is generated by the varying TIs experienced by that slice. Given a set of $TI_{j,k}$ values, the signal-intensity evolution for tissues with different T_1 values can be calculated using Bloch equation simulations, assuming mono-exponential relaxation, zero transverse magnetization, and ideal flip angles. After normalization of each vector, the calculated set of signal-intensity vectors for the chosen range of T_1 values can be assembled into a matrix $\mathbf{D}$, with one column per T_1 value, which forms the reconstruction dictionary. By finding the best-matching dictionary entry to the voxel-wise data acquired from the scanner using a pattern-matching algorithm, such as the vector dot product, the corresponding T_1 value can be identified and assigned to the voxel.

Slice-Ordering Optimization

Let N be the number of slices and K be the number of measurements. Optimizing the constant skip-factor slice ordering, $\boldsymbol{x}=[TI_{1,1},\ TI_{2,1},\ \ldots\ TI_{N,K}]$ can be accomplished using concepts originally developed for MRF schedule optimization (22–25). In MRF schedule optimization, an optimization dictionary is defined by selecting a range of T_1 values covering the anatomical range of interest representing different tissue types. The magnetization of each tissue is calculated using a Bloch simulation of the acquisition pulse sequence, and stored as a column vector that, after normalization of each vector, can be assembled into a matrix $\mathbf{H}$. The similarity between each vector in $\mathbf{H}$ and all others can be computed using the vector dot product. The diagonal elements of the dot product matrix $\mathbf{H}^T\mathbf{H}$ therefore measure the similarity between the signal from a tissue and itself, whereas the off-diagonal elements record the similarity with all other tissues, and a low dot product within these off-diagonal elements indicates high discriminability. The schedule of acquisition parameters can then be varied to find the ones that maximize the discriminability between tissues.

In this work, rather than varying the schedule of acquisition parameters, the slice ordering is varied instead. Varying the slice order in a given measurement is equivalent to varying the TI values sampled by each slice, such that each slice samples the signal at a subset of TI times out of the set of available TIs given by $(TR/N)\cdot(1, 2, \ldots, N)$. Because the slice ordering affects all slices simultaneously, the optimization dictionary must be expanded into a 3D matrix $\mathbf{H}_r$, in which r ranges from 1 to N to account for the effect on all slices. The goal of the optimization, however, remains the same: maximizing the discriminability or, equivalently, minimizing the similarity between tissues. The problem can therefore be recast as a search for the slice ordering that yields the lowest cost, defined here as the smallest sum of off-diagonal entries in each dot product matrix $(\mathbf{H}^T\mathbf{H})_r$. To avoid focusing the optimization on certain slices at the expense of others, the optimization problem is formulated as a search for the slice ordering that minimizes the maximum cost across all slices, as follows:

$$\min_{\boldsymbol{x}} \max_{\boldsymbol{r}} \sum_{i\neq j} ((\boldsymbol{H}^T\boldsymbol{H})_r)_{ij}(\boldsymbol{x}) \qquad [1]$$

This is equivalent to optimizing the discriminability of the "worst" (maximum cost) slice, although the current worst slice will change from iteration to iteration during the optimization, as the search space is explored.

Solving the Optimization Problem

Search-Space Reordering

Equation [1] represents an optimization over a set of permutations. Optimizing over permutations (i.e., the space of all possible orderings of a contiguous set of integers) is a challenging problem, and traditional optimization

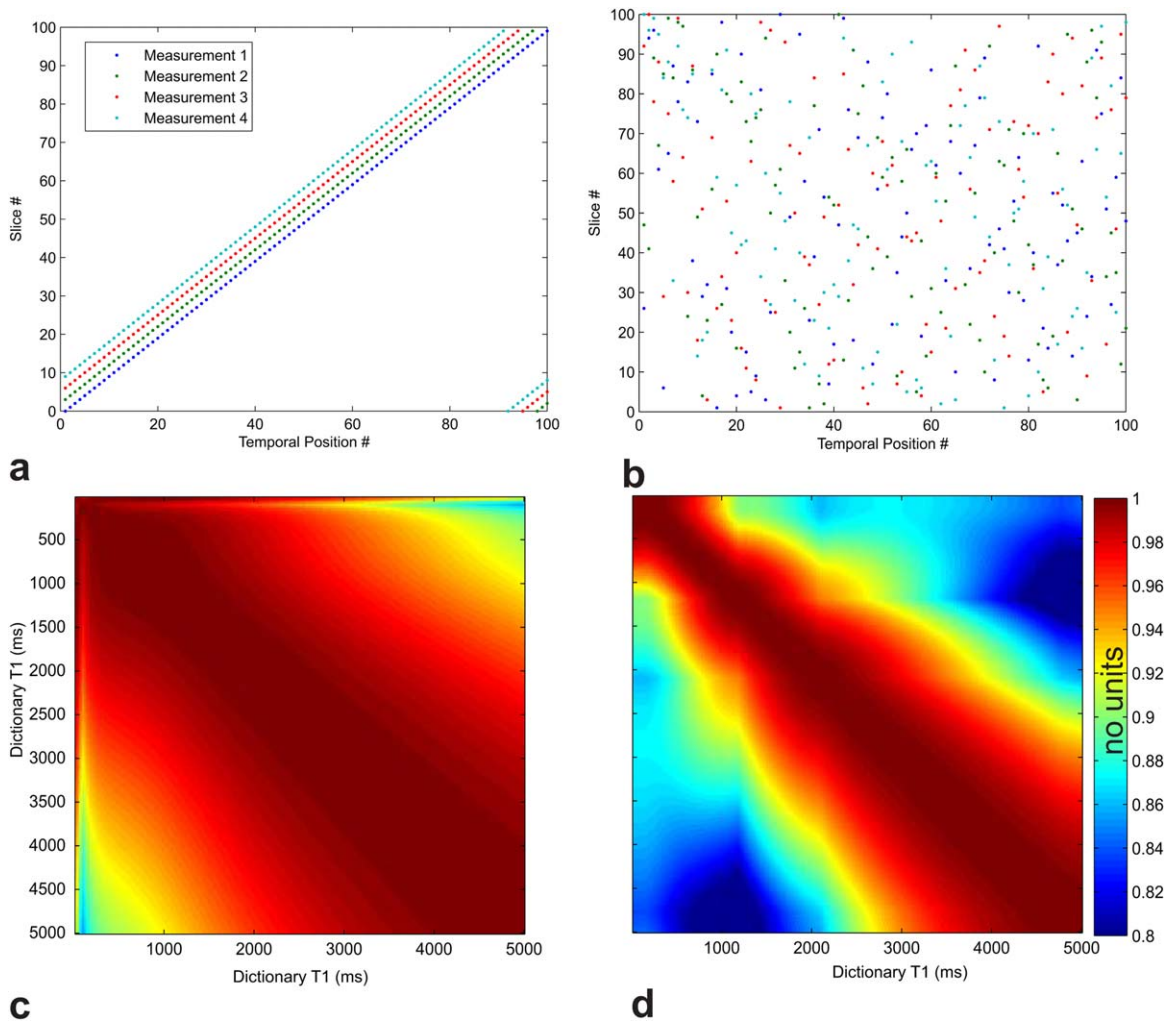

FIG. 1. Example orderings and corresponding dot-product matrices $\mathbf{H}^T\mathbf{H}$. **a**: The slice ordering for 100 slices corresponding to an optimized acquisition with skip factor of 3. The temporal order of the slice acquisition matches the anatomical order, but with each IR period, the starting slice index is incremented by 3 such that in the first IR period the acquisition starts with slice 0, in the second IR period the acquisition starts with slice 3, and so on. **b**: The slice orderings for 100 slices corresponding to an optimized acquisition in which the ordering is computed to maximize discriminability of the signal evolution across distinct tissues. **c**: The dot-product matrix $\mathbf{H}^T\mathbf{H}$ for a representative slice corresponding to the unoptimized case. The high values off the diagonal indicate poor discriminability. **d**: The dot product matrix $\mathbf{H}^T\mathbf{H}$ for the same slice corresponding to the optimized case shown in (**b**). Lower values off the diagonals of approximately 5% on average indicate improved discriminability.

algorithms are not designed for optimizing over permutation space, and are therefore ineffective. Genetic algorithms (26) may be used but require significant computational resources and processing time to converge to a solution. Instead, we apply a mapping to transform the unordered permutation search space into an ordered vector space (27). This mapping is performed by assigning an order to permutations. For example, an ordering can be defined for permutations of the ordered set of n integers $\boldsymbol{a}=\{a_1,a_2,\ldots,a_n\}$ through mapping to a new ordered set of integers $\boldsymbol{b}=\{b_1, b_2,\ldots,b_n\}$ defined such that b_i equals the number of elements of the set $\boldsymbol{a}$ preceding the location of $a_j=i$ that are greater than i (28). For example (taken from (28)), if $\{a_1, a_2, \ldots, a_8\}=\{5, 6, 1, 3, 2, 4, 8, 7\}$ then $\{b_1, b_2, \ldots, b_8\}=\{2, 3, 2, 2, 0, 0, 1, 0\}$. This mapping enables the use of faster algorithms that operate on vector spaces (29).

Dynamic Hill Climbing

Equation [1] can be solved using the dynamic hill climbing algorithm (28). The algorithm consists of searching the hyperspace for the point (slice ordering) that has the lowest cost as defined by Equation [1]. The algorithm is initialized with a slice ordering defined with a constant skip factor between measurements (Fig. 1a) used in previous work (9). This ensures that any slice ordering found will improve upon the constant skip-factor slice ordering. The algorithm explores the search space by defining a random probing vector, which is added to the initial point. If the new point improves on the current cost, the probing vector length is increased; otherwise it is decreased. This process is repeated until the probing vector length is below a certain threshold, at which point the algorithm moves to the next iteration. The point with the lowest cost found corresponds to the optimal slice

ordering (Fig. 1b) with the greatest discriminability (Figs. 1c and 1d).

METHODS

Optimization Cost

Optimized orderings for protocols consisting of 100 slices were generated by defining an optimization dictionary with T_1 values in the range of 100 to 5000 ms in intervals of 50 ms. Slice orderings were generated with 4, 5, 8, 10, and 16, measurements and their optimization costs (i.e., their discrimination) were compared. An additional 21-measurement ordering with a constant skip factor of 3 was used for comparison with our previously published protocol (9). Similar length slice orderings were generated for 25 and 50 slices, and their optimization costs were compared as well. The optimization algorithm was allowed to run for 50,000 iterations to ensure adequate coverage of the search space, which required approximately 8 to 40 h, depending on the slice-ordering length and the number of measurements, on a 2.4 GHz Core i7 Dell laptop with 16 GB RAM and 256 GB hard drive.

MRI

Phantom Experiments

For phantom experiments, a 3T Tim Trio (Siemens Healthcare, Erlangen, Germany) whole-body scanner was used with the manufacturer's body coil for transmit and 12-channel head array coil for receive. The TR/TI/echo time (TE)/bandwidth was set to 6690 ms/13 ms/27 ms/2170 Hz/pixel. The resolution was set to $1.2 \times 1.2 \times 1.2\,mm^3$ with a matrix of 192×192. An acceleration factor of $R = 4$ was used along with fast low-angle excitation echo-planar technique autocalibration (30,31) before acquisition, and the images were reconstructed online using the generalized autocalibrating partial parallel acquisition (32) method. A nonspatially selective adiabatic inversion pulse (33) ensured adequate inversion of the spins in the presence of spatial nonuniformity of transmit efficiency (as a result of dielectric effects).

In Vivo Human Experiments

For human experiments, the same TR/TI/TE/R/bandwidth and resolution were used as in the phantom experiments, but with a 32-channel head array for reception. The total scan time for the 4, 5, 8, 10, 16, and 21 measurements was 33, 40, 60, 74, 114, and 147 s, respectively. For the same spatial coverage, a $1 \times 1 \times 1\,mm^3$ isotropic acquisition would require an additional 6 to 8 s for each scan. Although fat suppression is commonly used in EPI experiments to avoid chemical shift artifacts, in this work fat suppression was disabled in all in vivo experiments to avoid biasing the T_1 quantification (see subsequent sections for an explanation of the fat suppression bias).

Estimation of T_1 Values

All data were estimated by calculating the voxel-wise dot product between the acquired data and the entries of the precomputed dictionary of signal magnetizations, and selecting the best match. The dictionary consisted of T_1 values in the range of 1 to 5000 ms in intervals of 1 ms.

Phantom

The accuracy and precision of the optimized slice orderings was assessed using the International Society for Magnetic Resonance in Medicine (ISMRM)/National Institute of Standards and Technology (NIST) multicompartment phantom with calibrated T_1 and T_2 values similar to those of the human brain (34). The phantom was scanned with the 8-measurement slice ordering, and the resulting T_1 maps compared to both the true phantom values (characterized by NIST and calculated using the gold-standard NMR spectroscopy IR sequence) and the unoptimized 21-measurement protocol. Two phantom compartments with the shortest T_1 values (< 30 ms) were excluded from the measurements, as their T_1 were comparable with the TE of the EPI sequence.

To rule out any scanner-specific biases, we also validated the true phantom values using the recommended IR method based on a nonselective IR spin-echo (IR-SE) EPI acquisition. The TR was set to 18 s and TE set to 21 ms. The minimum TI available for this sequence was 21 ms. A logarithmically spaced sampling of 36 TI values was used to ensure accurate fitting of the short T_1 compartments. Total scan time for the 36 TIs was approximately 65 min. The magnitude-valued images were fitted to the three-point inversion-recovery signal equation (Ref. (8)) using the Levenberg-Marquadt algorithm (`lsqcurvefit` function) in MATLAB (The MathWorks, Natick, MA).

Fat Suppression

Because fat suppression pulses may affect the T_1 quantification through, for example, magnetization transfer [9,35], the acquisition was repeated both with and without fat suppression pulses for the 8-measurement length. The frequency profile of the fat suppression pulse used on the scanner was computed using a custom-made Bloch equation simulator written in MATLAB to determine its potential effect on the water signal (through inadvertent excitation of the water peak).

Slice-Specific Optimization Cost

Because the optimization algorithm uses a single global metric to converge to an optimal slice ordering, once the algorithm converges, different slices can have different optimization costs. The resulting slice-specific cost of the optimized 8-measurement protocol was therefore compared with that of the unoptimized 21-measurement protocol.

In Vivo Human

A healthy 29-year-old male subject was recruited for this study and provided informed consent prior to the experiment in accordance with our institution's Human Research Committee.

Validation

The T_1 map obtained with our method was validated in vivo in a single slice using the same recommended IR-SE EPI sequence and protocol described previously. The total scan time for this one slice sampled at 36 TIs was approximately 65 min. Three regions corresponding to gray matter, white matter, and cerebrospinal fluid (CSF) were selected from each image, and the agreement between the mean T_1 values of each region was assessed.

Reproducibility

A mask was created to remove all signals extraneous to the head by summing the signal from the 21-measurement protocol and thresholding the resulting volume. The masked T_1 maps from the initial and subsequent scans were coregistered in MATLAB (imregister function) and used to calculate the correlation coefficient for different measurement lengths as a measure of the reproducibility/precision of the estimated in vivo T_1 values. The correlation coefficient was calculated including the CSF from the whole brain. However, we also calculated the correlation coefficient with the CSF removed by thresholding the T_1 maps to remove all voxels with T_1 greater than 2000 ms.

Following coregistration, spatial variations in the reproducibility were measured for the 8-measurement acquisition by calculating the slice-specific correlation coefficient.

RESULTS

Optimization Cost

The $(\mathbf{H}^T\mathbf{H})_r$ matrix from a representative slice for a 100-slice unoptimized 21-measurement protocol is shown in Figure 1c in comparison with an optimized 8-measurement protocol (Fig. 1d). The off-diagonal elements in the optimized matrix are approximately 5% smaller on average than those of the unoptimized matrix, which indicates improved discriminability in the optimized case.

The relationship between the cost of the optimization function and the number of measurements (acquisition length) is shown in Figure 2 for example orderings with 25, 50, and 100 slices. The optimization cost for slice orderings with fewer slices was correspondingly smaller, as expected, given the smaller slice-ordering search space. Importantly, for a given number of slices, the cost of the unoptimized 21-measurement protocol was higher than that of the optimized protocols with a smaller number of measurements.

Phantom

The accuracy of the proposed approach was assessed by estimating T_1 values in the calibrated ISMRM/NIST phantom. The measured and true T_1 values for the optimized 8-measurement and unoptimized 21-measurement acquisition are shown in Figure 3. The measured T_1 values were derived from the average T_1 value estimated from within each compartment. Compartments with T_1 values similar to the TE of the EPI ($T_1 < 30$ ms) showed

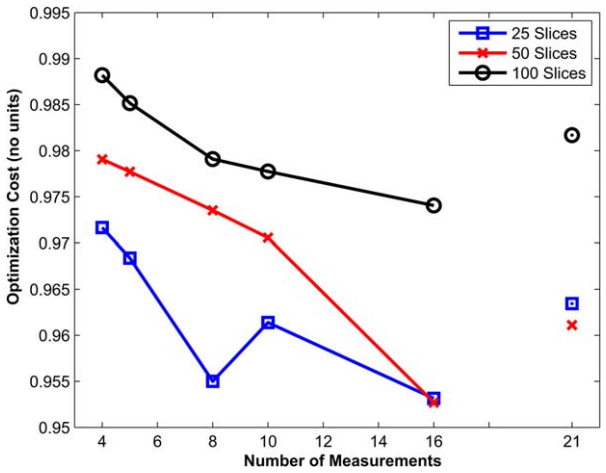

FIG. 2. Cost of the optimization objective function for increasing number of measurements (acquisition duration) for example slice orderings with 100 (black circles), 50 (red crosses), and 25 (blue squares) slices. Note that a smaller number of slices resulted in lower cost (i.e., superior discrimination) as a result of the smaller search space.

significant error in both protocols, as expected, and were not included in the calculations of the comparison metrics. Such short T_1 values may not be estimable with the current EPI readout. The Pearson correlation coefficient R was calculated for each acquisition, resulting in an R^2 value of 0.99 for both acquisition methods tested. However, the linear fit shows a small offset of 0.74 ms for the 8-measurement protocol, and for the 21-measurement protocol an offset of 19 ms was calculated, indicating a negligible estimation bias associated with this protocol. Unlike the identical R^2 values, the root mean-squared error for the 8-measurement protocol was 31 ms, which was lower than the 40 ms calculated for the 21-measurement protocol. The estimation of absolute error, defined as |Estimated – True|, as a function of the reference T_1 values for each protocol, was also calculated and is shown in Figures 3c and 3d. The mean error across all compartments (excluding the short T_1 compartments) was found to be 25 ms for the optimized 8-measurement acquisition and 33 ms for the unoptimized 21-measurment acquisition. Despite the approximate three-fold reduction in scan time, the 8-measurement protocol showed excellent agreement with the true phantom values. The measured and true T_1 values for the IR-SE EPI sequence are shown in Figure 4. In contrast to the 8-measurement protocol, which correctly reconstructed compartments with T_1 values as short as 30 ms, the IR-SE EPI sequence showed significant errors for compartments with T_1 values shorter than 100 ms, which therefore were not included in the R^2 or root mean-squared-error calculations. However, the remaining compartments showed excellent agreement with the true phantom values ($R^2 = 0.99$), a negligible estimation bias (an offset of 1.7 ms) and a root mean-squared error of 12 ms, demonstrating that any scanner-specific biases are minimal.

Fat Suppression

The presence of the fat-suppression pulse increased the error in the measured T_1 values (Figs. 5a and 5b),

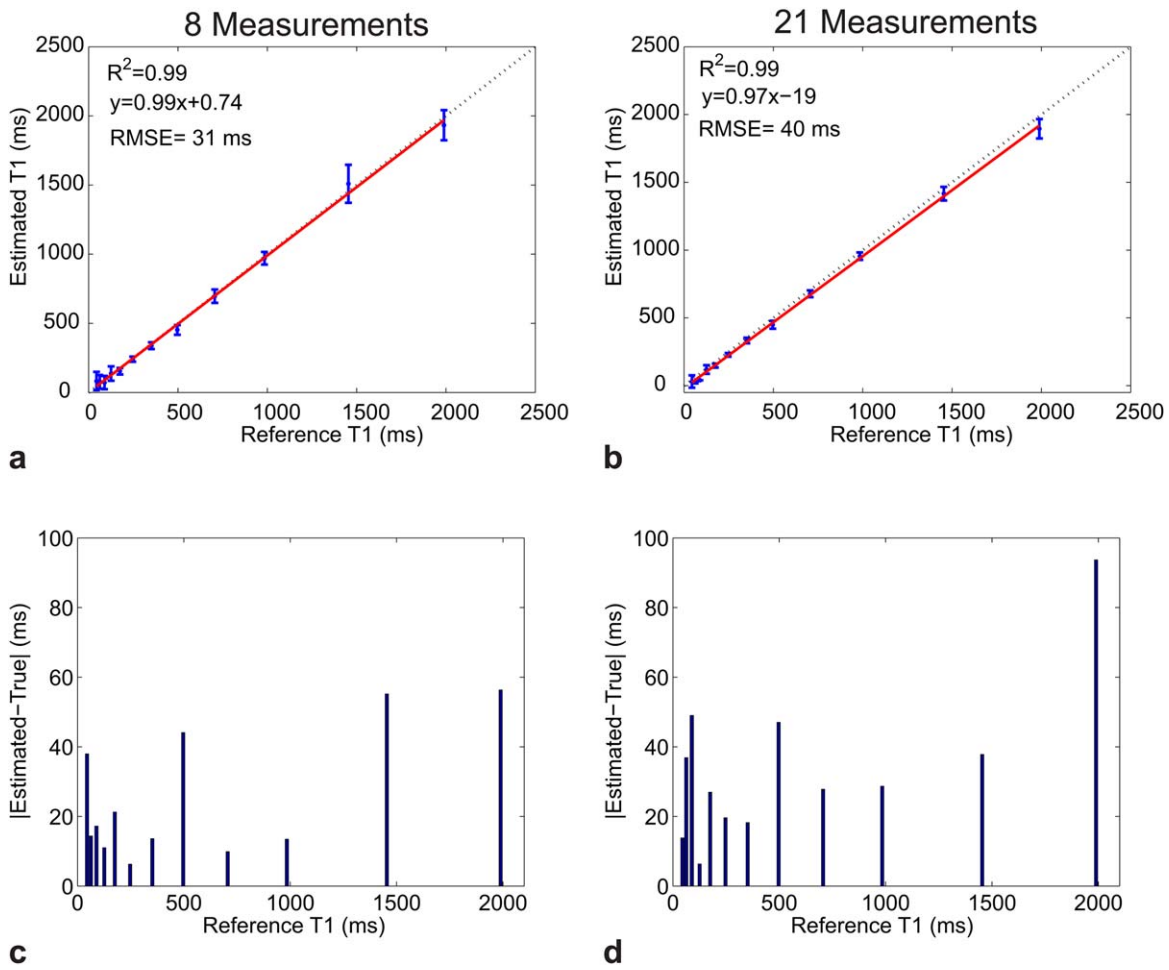

FIG. 3. T_1 estimation accuracy evaluated in the calibrated ISMRM/NIST phantom. Shown is a comparison between the true and measured compartment T_1 values for an optimized 8-measurement protocol (**a**) and an unoptimized 21-measurement protocol (**b**). The dashed line in each plot is the identity line, whereas the red line is the least-squares-fit line. The error bars represent the standard deviation of the measured T_1 values within the compartment. Note the larger bias in the 21-measurement protocol. The estimation errors as a function of the reference phantom T_1 values are shown in (**c**) for the 8-measurement protocol and in (**d**) for the 21-measurement protocol.

particularly for long T_1 compartments. Specifically, the root mean-squared error for the 8-measurement protocol was 76 ms for acquisitions with fat suppressions, but 31 ms for those without fat suppression. Although the fat-suppression pulse is centered on the frequency corresponding to the lipid chemical shift, the simulated frequency profile (Fig. 5c) showed that approximately 2% of the water signal is also excited (and subsequently dephased) for each slice-selective excitation.

Slice-Specific Optimization Cost

The optimization cost of each slice for an 8-measurement acquisition is shown in Figure 6a, and that of the 21-measurement protocol is shown in Figure 6b. Because each slice is assigned a distinct acquisition schedule, and thus a distinct collection of TI values, each slice in the acquisition has a somewhat different cost in the final schedule generated from the optimization. The slice-optimization cost can thus provide a metric for a priori confidence in, or for predicting the expected accuracy of, the T_1 estimates and a guide to

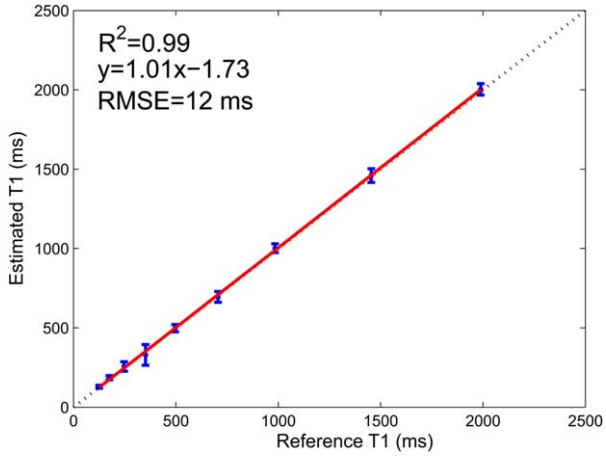

FIG. 4. Comparison of the ISMRM/NIST calculated phantom T_1 values to those of a nonselective IR-SE EPI sequence. The true and measured compartment T_1 values are shown along with the identity line (dashed line) and the least-squares-fit line (red line). Note that compartments with T_1s smaller than 100 ms showed significant error and were not included in the comparison.

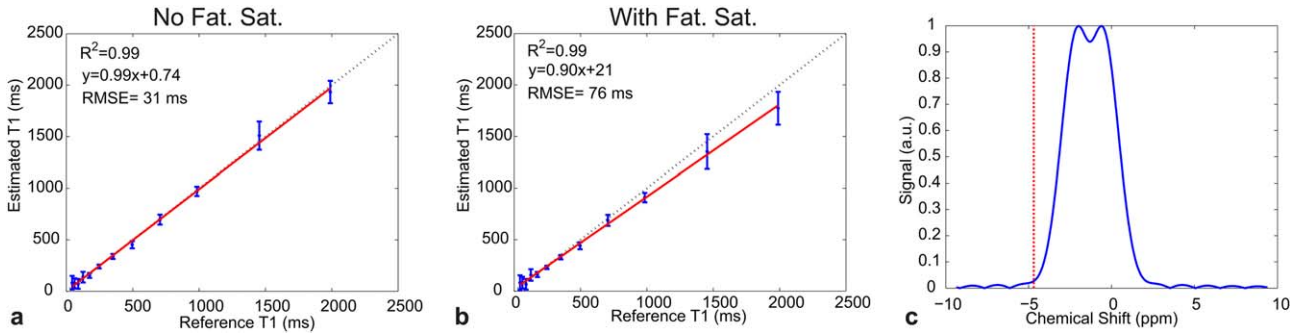

FIG. 5. True and measured compartment T_1 values calculated from calibrated ISMRM/NIST phantom data for the optimized 8-measurement protocol without (**a**) and with (**b**) the presence of a fat-saturation pulse. The dashed line is the identity line, whereas the red line is the least-squares-fit line. The fat saturation pulse (**c**) centered on the lipids chemical shift nevertheless excites approximately 2% of the water signal for every slice-selective excitation pulse. The deviation from the identity line is larger in the fat-suppression case.

judge whether the optimization process, which may terminate within a local minimum, should be allowed to continue, to further reduce the estimation error. (See the "Discussion" for a consideration of the potential uses for this ability to predict estimation error.)

As each slice also samples a distinct set of TI values, for each 100-slice protocol we calculated the range of TI values (defined as the maximum TI minus the minimum TI) for each slice, then summarized the effect of the number of measurements on the range of TI values by the mean and standard deviation of the range across all slices. The results of this calculation are presented in Supporting Table S1. For the optimized slice orderings, as expected, the mean TI value range increases with an increasing number of measurements, whereas the standard deviation decreases. The mean range of TI values was similar for the optimized 8-measurement protocol and the unoptimized 21-measurement protocol, but the standard deviation of the range of TI values was lower in nearly all of the optimized protocols compared with the unoptimized 21-measurement protocol, indicating that the ranges of TI values sampled in the optimized protocols were more consistent across slices.

In Vivo Human Brain

Reconstructed T_1 maps for the 8-measurement protocol of the 100-slice case are shown in Figure 7 for three different example slices, along with a histogram of each slice's calculated T_1 values. The various visible peaks in the histograms (Figs. 7d–7f) correspond to literature values of T_1 at 3 T (36) of the white matter (~900 ms), gray matter (~1600 ms), and CSF (~4000 ms) tissues, further validating the proposed method. Gaps in the histograms of the different slices are in part a result of anatomical features (e.g., scalp, CSF) that are less prevalent in some slices, leading to low voxel counts for the corresponding T_1 values, as well as slice-dependent fitting inaccuracies described in the "Calculating Expected T_1 Mapping Accuracy From the Dictionary Discrimination" section. A comparison of the same slice for the 100, 50, and 25 slices case for 4, 8, and 21 measurements is shown in Figure 8 (remaining measurements are shown in Supporting Fig. S1). The T_1 maps of the entire volume for all measurement lengths tested are shown in Supporting Figures S2 to S7. The proton density (PD) weighted S_0 maps obtained with the optimized 8-measurement protocol in comparison with those of the unoptimized

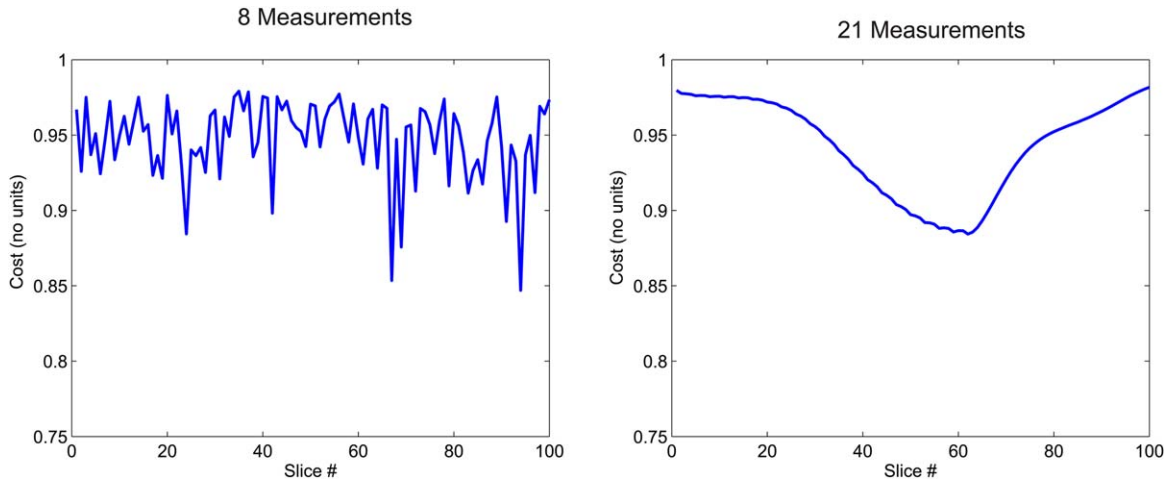

FIG. 6. Optimization cost of each slice for an 8-measurement acquisition (**a**) and an unoptimized 21-measurement acquisition (**b**). Higher cost indicates lower discrimination between different T_1 values that may lead to increased error in the reconstructed T_1 maps.

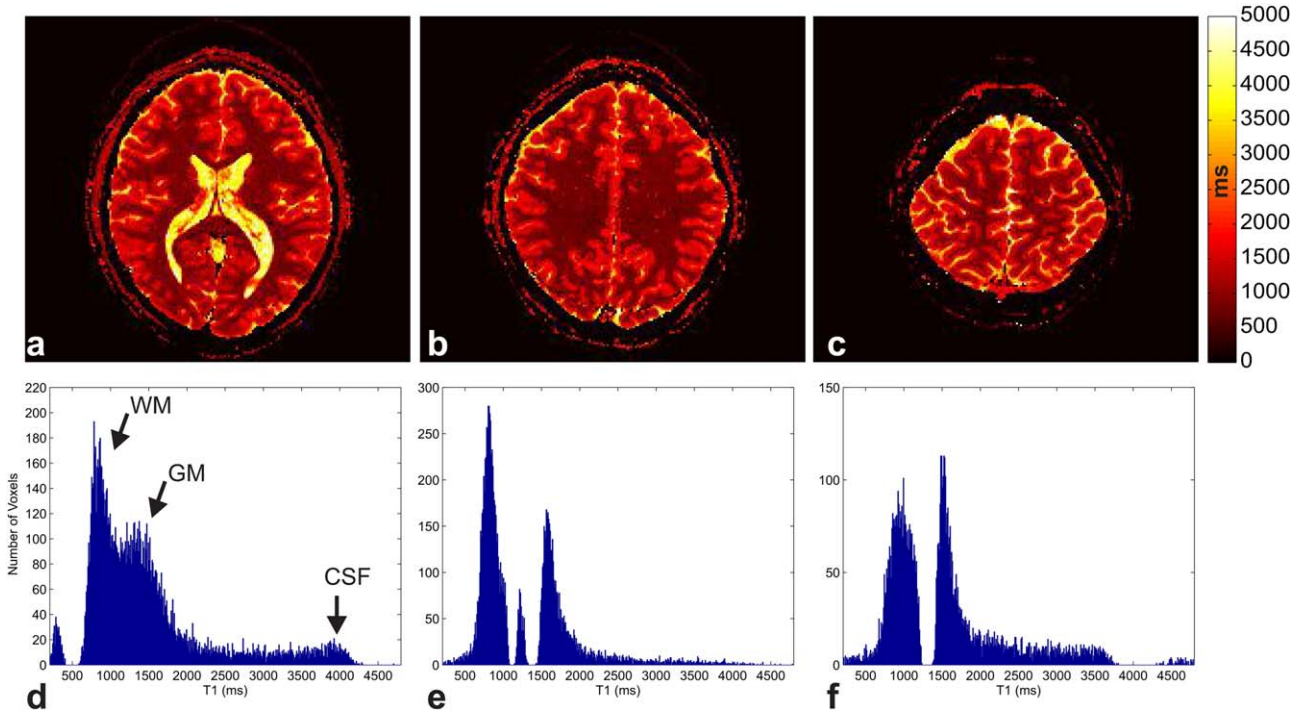

FIG. 7. Example quantitative T_1 maps within the brain for three sample slices (**a**–**c**) out of the optimized 8-measurement 100-slice acquisition. The color scale indicates the T_1 value in units of ms. The histogram of T_1 values for each slice shown in (**d**–**f**) shows distinct peaks corresponding to the white matter, gray matter, and CSF.

21-measurement protocol are shown in Supporting Figure S8, and demonstrate the close similarity between the two maps, which were estimated using the optimized and unoptimized protocols.

Validation

The T_1 map from a single slice estimated by the recommended IR-SE sequence is shown in Figure 9 in comparison with that obtained with the proposed method. The mean $\pm$ standard deviation of gray matter, white matter, and CSF T_1 values from the recommended IR-SE sequence were 767 ± 16.0, 1130 ± 47.0, and 4120 ± 264 ms, respectively, and showed good agreement with the 767 ± 74.0, 1160 ± 96.0, and 3830 ± 299 ms values, which were estimated with the proposed 8-measurement protocol. We also attempted to register the single-slice T_1 map from the recommended IR-SE sequence to the same-session T_1 EPI data, and within this slice found an R^2 value of 0.64 across all voxels. The R^2 value for the same comparison based on the NIST/ISMRM phantom was 0.99 over a similar range of T_1 values, suggesting some loss of agreement as a result of participant motion and misalignment.

Reproducibility

The variation in the correlation coefficient as a function of the number of measurements is shown in Figure 10a for the across- and within-session acquisitions. The CSF was included in this calculation, as its removal had a negligible effect on the correlation coefficient. The within-session correlation coefficient is, on average, approximately 2% higher than the across-session coefficient, likely because of the smaller shift in head position between within-session scans compared with across-session scans. Because there is a slice-specific T_1 estimation error, differential head motion between scans will reduce the precision of the estimate. Both coefficients show an increase in the correlation coefficient with increasing number of measurements, reaching a value of approximately 0.90 for the within-session 8-measurement protocol used in this study. The within-session correlation coefficient for the 21-measurement protocol was an outlier at approximately 0.88, which is slightly lower than expected given the approximate 0.91

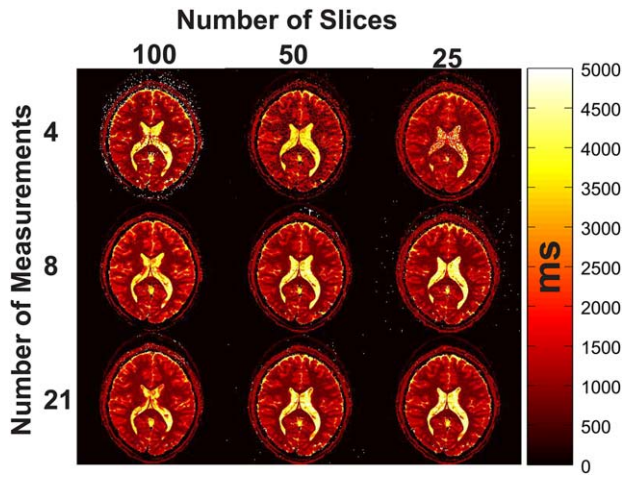

FIG. 8. Reconstructed T_1 maps for a representative slice for 4, 8, and 21 measurements for the 100, 50, and 25 slices case.

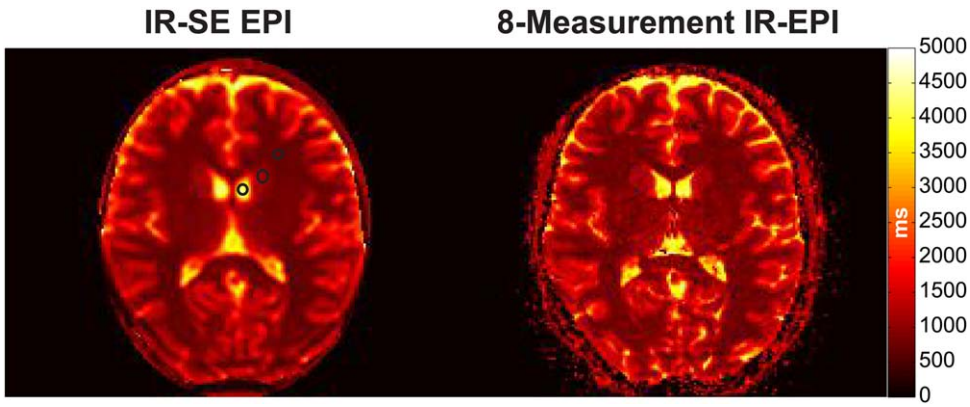

FIG. 9. In vivo T_1 map from a single slice estimated with the recommended IR-SE sequence in comparison to the T_1 map obtained with the 8-measurement optimized protocol for the same slice. The black circles indicate the locations of the gray matter, white matter, and CSF regions used to compare the agreement between the two methods.

across-session coefficient. This is likely caused by the abrupt subject motion observed before this run.

The spatial variation in the within-session slice-specific correlation coefficient for the 8-measurement acquisition is shown in Figure 10b. As expected, slices outside the brain containing little tissue yielded the minimum correlation of approximately 0.43. In contrast, slices in the center of the brain showed the greatest reproducibility with a correlation coefficient of approximately 0.96.

DISCUSSION

We have demonstrated that optimization of the slice ordering can maximize discrimination between different tissues, to allow accurate reconstruction of the quantitative T_1 maps despite reduced scan time. The accelerated 8-measurement protocol EPI acquisition allows distortion-matched whole-brain quantitative T_1 mapping in approximately 60 s. However, several factors may affect the quality of the derived maps, as described subsequently.

Reconstruction Dictionary

Because the signal in each voxel is matched to the precomputed dictionary, factors that affect the generated dictionary entries may introduce bias into the reconstructed T_1 maps. In particular, the dictionary construction assumed an ideal 180° inversion pulse and zero-transverse magnetization, which may not hold in reality as a result of spatial variations in the B_1^+ transmit field. These concerns are mitigated, however, by the use of adiabatic inversion pulses that are largely immune to B_1^+ inhomogeneity. Note that errors in the excitation flip angle do not affect the recovery rate, and therefore do not influence the T_1 value estimation and are accounted for by the dictionary normalization. The slice-selective excitation pulses used in our multiple-slice acquisition may introduce biases as well, due to off-resonance effects on neighboring slices, such as incidental magnetization transfer (8,37). Nevertheless, the variable slice ordering (Fig. 1b) may impart additional robustness to this form of bias as well, as the time between excitation of a given slice and the measurement of its neighboring slices, which determines the amount of inadvertent magnetization transfer from the slice-selective excitation pulses, will be

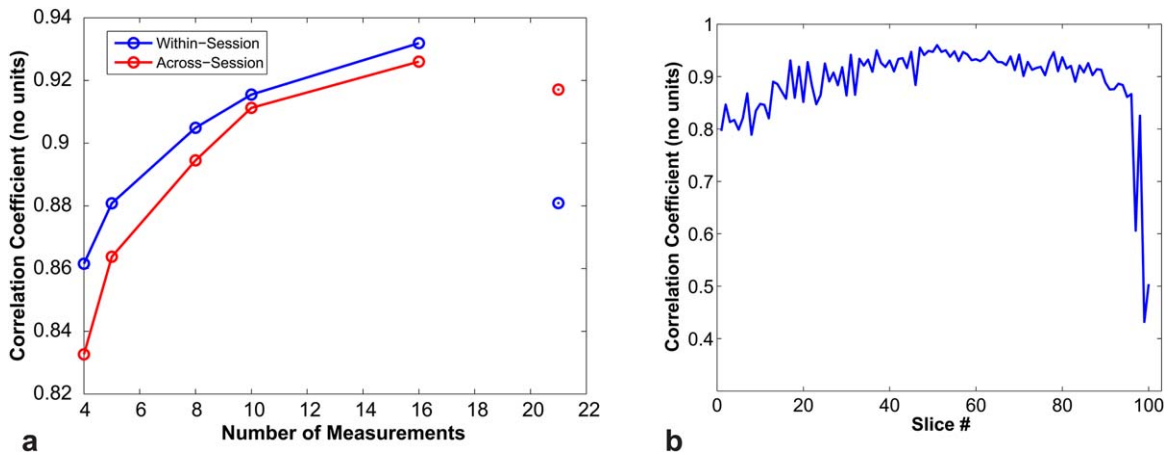

FIG. 10. **a**: The scan–rescan correlation coefficient as a function of the number of measurements for the across- and within-session acquisitions. The optimized acquisitions show good repeatability despite a significantly shorter scan length. **b**: The within-session, slice-specific correlation coefficients for the 8-measurement protocols illustrate the spatial variation of the correlation coefficient.

different from one inversion recovery period to the next, and may therefore average out provided a sufficient number measurements. The minimal bias seen in the reconstructed T_1 maps for the optimized protocol (less than 1 ms), as shown in Figure 3, validates the assumptions made in the dictionary construction, but it is possible that other sources of bias remain.

Optimization Algorithm

A set of N slices allows a factorial of N (i.e., $N!$) possible permutations of the ordering. The immensity of the search space for $N > 10$ precluded a brute-force search for the globally optimal slice ordering, and required the use of optimization algorithms. This problem can be formulated as a variation of the traveling salesman problem (38), a problem that has been studied intensively and for which multiple heuristics and algorithms exist (39–41). In this study, we used a hill climbing algorithm to search for a local optimum because of its simplicity and speed. More sophisticated algorithms are likely to provide a more globally optimal solution and are the subject of ongoing research.

In general, fewer slices will entail a smaller search space, making it more likely for the optimization algorithm to find an ordering with lower cost, as shown in Figure 2. This suggests that incorporating slice-acceleration techniques, such as simultaneous multislice EPI (42–44), as proposed previously for IR-EPI (17,18), which effectively reduces the number of slices, may provide lower cost and therefore higher accuracy—assuming the acquisition has a sufficient signal-to-noise ratio. Of note, the acquisition of multiple slices incurs no signal-to-noise ratio penalty for simultaneous multislice EPI acquisitions other than g-factor reconstruction noise (45). It is important to recall that the size of the search space is defined by the product of the effective number of slices and the number of measurements, both of which constitute degrees of freedom for the protocol optimization. Because the algorithm is based on a local search, it is possible for it to converge to a local minimum, which may be more likely if either the effective number of slices or the number of measurements is large. Put simply, for a given number of slices, finding the optimal ordering for acquisitions with a larger number of measurements will be more difficult. For simultaneous multislice acquisitions, although the image reconstruction can generate a larger number of slices than conventional EPI methods, the effective number of slices is not increased; therefore, a 126-slice acquisition with conventional EPI, for example, is expected to typically have higher cost and increased estimation error than an equivalent 126-slice acquisition collected with simultaneous multislice techniques. This extension of our approach to simultaneous multislice acquisitions will be explored in future work.

Calculating Expected T_1 Mapping Accuracy From the Dictionary Discrimination

In its current implementation, the optimization routine searches for a slice ordering that minimizes a single objective: the maximum cost across all slices. Therefore, the slice ordering obtained, although optimal in a global sense, may yield a solution with a variable cost for every individual slice. Indeed, plotting the cost for each slice in an optimized 8-measurement acquisition shows significant variation between the discrimination of each individual slice (Fig. 6a). A similar, albeit smoother, variation exists in the slice-specific cost of the 21-measurement acquisition (Fig. 6b) with a constant skip-factor scheme. Consequently, the dictionary-matching reconstruction in certain slices will be more robust to errors than in other slices. This is evident in the histograms shown in Figures 7d to 7f, in which the estimation error leads to gaps in the voxel count of certain T_1 values. As demonstrated by the phantom experiments (Fig. 5), this error is small and zero-mean across slices, and, importantly, can be predicted from each slice's optimization cost (Fig. 6). Additionally, it should be noted that slice orderings with a high cost can still yield accurate T_1 maps, provided the signal-to-noise ratio is sufficiently high to allow distinguishing similar signal evolutions. Nevertheless, for a given signal-to-noise-ratio level, the optimization cost can be used as an a priori measure of the expected quality of the estimated T_1 map for the given slice, and the optimization can be further iterated as needed to minimize the cost for the particular slice. Alternatively, multi-objective optimization techniques can be used (46,47) to find a slice ordering that minimizes the cost for all slices simultaneously.

Effect of Fat Saturation

The imperfect frequency profile of the fat-saturation pulse used resulted in undesired excitation and dephasing of approximately 2% of the total water signal for every slice-selective excitation, given the nonspatially selective nature of the pulse. This effect explains the results shown in Figure 5, in which the cumulative effect of the fat-suppression pulse is particularly pronounced for phantom compartments with long T_1, given their long recovery time. This effect could be modeled and incorporated into the Bloch simulation during the dictionary generation, to account for this effect in the phantom data. However, inadvertent magnetization transfer from tissue macromolecules could still contribute to biasing T_1 values in vivo, as discussed previously (48). Because these magnetization transfer effects are presumably constant over time and accumulate linearly during each IR period, it is possible to model these effects as well (9); to simplify the modeling in this work, we opted to forgo the fat-saturation pulse, resulting in small amounts of chemical shift artifact in the data.

Potential Future Applications

Quantitative T_1 mapping is important in numerous applications. Dynamic contrast-enhanced MRI is commonly used for with pharmacokinetic models to calculate permeability parameters of tumors and other lesions (49). T_1-weighted images are used in practice rather than the quantitative T_1 maps, due to the lengthy acquisition times. Because T_1-weighted images are susceptible to confounding factors and bias, this can have a deleterious

effect on the accuracy of the perfusion maps obtained. Fast quantitative T_1 mapping provided by the proposed method would remove this source of error and yield more accurate tissue-permeability maps.

CONCLUSIONS

We have demonstrated a method for optimizing the TIs used in multi-inversion EPI. The optimized TIs provide similar precision and accuracy in less time, allowing an approximate three-fold reduction in the scan time needed to obtain the quantitative tissue maps, as shown in phantom and in a healthy human subject scanned at 3 T.

ACKNOWLEDGMENTS

We thank Drs. Ville Renvall and Thomas Witzel for providing the IR-EPI pulse sequence software, Dr. Karl Stupic for providing the ISMRM/NIST phantom, and Mr. Ned Ohringer for assistance with scanning.

REFERENCES

1. Clare S, Jezzard P. Rapid T1 mapping using multislice echo planar imaging. Magn Reson Med 2001;45:630–634.
2. de Smit F, Hoogduin H. Fast whole brain T1 mapping at 3 Tesla. RöFo-Fortschritte Auf Dem Geb. Röntgenstrahlen Bildgeb. Verfahr, vol. 177; 2005, p A1.
3. Ordidge R, Gibbs P, Chapman B, Stehling M, Mansfield P. High-speed multislice T1 mapping using inversion-recovery echo-planar imaging. Magn Reson Med 1990;16:238–245.
4. Look DC, Locker DR. Time saving in measurement of NMR and EPR relaxation times. Rev Sci Instrum 1970;41:250–251.
5. Gowland P, Mansfield P. Accurate measurement of T1 in vivo in less than 3 seconds using echo-planar imaging. Magn Reson Med 1993;30: 351–354.
6. Henderson E, McKinnon G, Lee T-Y, Rutt BK. A fast 3D Look-Locker method for volumetric T 1 mapping. Magn Reson Imaging 1999;17: 1163–1171.
7. Stikov N, Boudreau M, Levesque IR, Tardif CL, Barral JK, Pike GB. On the accuracy of T1 mapping: searching for common ground. Magn Reson Med 2015;73:514–522.
8. Barral JK, Gudmundson E, Stikov N, Etezadi-Amoli M, Stoica P, Nishimura DG. A robust methodology for in vivo T1 mapping. Magn Reson Med 2010;64:1057–1067.
9. Renvall V, Witzel T, Wald LL, Polimeni JR. Automatic cortical surface reconstruction of high-resolution T 1 echo planar imaging data. NeuroImage 2016;134:338–354.
10. Kwong KK, Belliveau JW, Chesler DA, et al. Dynamic magnetic resonance imaging of human brain activity during primary sensory stimulation. Proc Natl Acad Sci 1992;89:5675–5679.
11. Kwong KK, Chesler DA, Weisskoff RM, et al. MR perfusion studies with T1-weighted echo planar imaging. Magn Reson Med 1995;34: 878–887.
12. Jezzard P, Balaban RS. Correction for geometric distortion in echo planar images from B0 field variations. Magn Reson Med 1995;34:65–73.
13. Mugler JP, Brookeman JR. Three-dimensional magnetization-prepared rapid gradient-echo imaging (3D MP RAGE). Magn Reson Med 1990; 15:152–157.
14. Marques JP, Kober T, Krueger G, van der Zwaag W, Van de Moortele P-F, Gruetter R. MP2RAGE, a self bias-field corrected sequence for improved segmentation and T 1-mapping at high field. NeuroImage 2010;49:1271–1281.
15. van der Zwaag W, Buur P, Versluis M, Marques JP. Distortion-matched T1-maps and bias-corrected T1w-images as anatomical reference for submillimeter-resolution fMRI. In Proceedings of the 24th Annual Meeting of the ISMRM, Singapore, 2016. Abstract 71.
16. Huber L, Marrett S, Handwerker DA, et al. Fast dynamic measurement of functional T1 and grey matter thickness changes during brain activation at 7T. In Proceedings of the 24th Annual Meeting of the ISMRM, Singapore, 2016. Abstract 633.
17. Grinstead JW, Wang D, Bhat H, et al. Slice-accelerated inversion recovery T1 mapping. In Proceedings of the 22nd Annual Meeting of the ISMRM, Milan, Italy, 2014. p 2318.
18. Dougherty R, Mezer A, Zhu K, Kerr A, Middione A. Fast quantitative T1 mapping with simultaneous multi-slice EPI. 20th Annual Meeting of the Organization for Human Brain Mapping, Hamburg, Germany, 2014. p. 2002.
19. Renvall V, Witzel T, Wald LL, Polimeni JR. Fast variable inversion-recovery time EPI for anatomical reference and quantitative T1 mapping. In Proceedings of the 22nd Annual Meeting of the ISMRM, Milan, Italy, 2014. p. 4282.
20. Kashyap S, Ivanov D, Havlicek M, Poser BA, Uludag K. High-resolution T1-mapping using inversion-recovery EPI and application to cortical depth-dependent fMRI at 7 Tesla. In Proceedings of the 24th Annual Meeting of the ISMRM, Singapore, 2016. Abstract 70.
21. Ma D, Gulani V, Seiberlich N, et al. Magnetic resonance fingerprinting. Nature 2013;495:187–192.
22. Cohen O, Sarracanie M, Armstrong BD, Ackerman JL, Rosen MS. Magnetic resonance fingerprinting trajectory optimization. In Proceedings of the 22nd Annual Meeting of the ISMRM, Milan, Italy, 2014. p 27.
23. Cohen O, Armstrong BD, Sarracanie M, Farrar, Christian T, Ackerman Jerome L, Rosen Matthew S. 15T ultrahigh field fast MR fingerprinting with optimized trajectories. In Proceedings of the 22nd Annual Meeting of the ISMRM, Milan, Italy, 2014. p 4285.
24. Cohen O, Sarracanie M, Rosen MS, Ackerman JL. In vivo optimized MR fingerprinting in the human brain. In Proceedings of the 24th Annual Meeting of the ISMRM, Singapore, 2016. p 430.
25. Cohen O, Rosen MS. Algorithm comparison for schedule optimization in MR fingerprinting. Magn Reson Imaging 2017. doi: 10.1016/j.mri.2017.02.010.
26. Davis L. Handbook of genetic algorithms. New York: Van Nostrand Reinhold; 1991.
27. Knuth DE. The art of computer programming: sorting and searching, vol. 3. London: Pearson Education; 1998.
28. Turrini S. Optimization in permutation spaces. Palo Alto, CA, USA: Western Research Laboratory; 1996.
29. Yuret D, De La Maza M. Dynamic hill climbing: overcoming the limitations of optimization techniques. In Proceedings of the 2nd Turkish Symposium on Artificial Intelligence and Neural Networks, Istanbul, Turkey, 1993. pp 208–212.
30. Chapman B, Turner R, Ordidge RJ, et al. Real-time movie imaging from a single cardiac cycle by NMR. Magn Reson Med 1987;5:246–254.
31. Polimeni JR, Bhat H, Witzel T, et al. Reducing sensitivity losses due to respiration and motion in accelerated echo planar imaging by reordering the autocalibration data acquisition. Magn Reson Med 2016; 75:665–679.
32. Griswold MA, Jakob PM, Heidemann RM, et al. Generalized autocalibrating partially parallel acquisitions (GRAPPA). Magn Reson Med 2002;47:1202–1210.
33. Ordidge RJ, Wylezinska M, Hugg JW, Butterworth E, Franconi F. Frequency offset corrected inversion (FOCI) pulses for use in localized spectroscopy. Magn Reson Med 1996;36:562–566.
34. Keenan KE, Stupic KF, Boss MA, et al. Multi-site multi-vendor comparison of T1 measurement using ISMRM/NIST system phantom. In Proceedings of the 24th Annual Meeting of the ISMRM, Singapore, 2016. p 3290.
35. Shin W, Gu H, Yang Y. Incidental magnetization transfer contrast by fat saturation preparation pulses in multislice Look-Locker echo planar imaging. Magn Reson Med 2009;62:520–526.
36. Bojorquez JZ, Bricq S, Acquitter C, Brunotte F, Walker PM, Lalande A. What are normal relaxation times of tissues at 3 T? Magn Reson Imaging 2017;35:69–80.
37. Dixon WT, Engels H, Castillo M, Sardashti M. Incidental magnetization transfer contrast in standard multislice imaging. Magn Reson Imaging 1990;8:417–422.
38. Hoffman KL, Padberg M, Rinaldi G. Traveling salesman problem. In: Encyclopedia of Operations Research and Management Science. New York: Springer; 2013, pp 1573–1578.
39. Dorigo M, Gambardella LM. Ant colony system: a cooperative learning approach to the traveling salesman problem. IEEE Trans Evol Comput 1997;1:53–66.

40. Černý V. Thermodynamical approach to the traveling salesman problem: an efficient simulation algorithm. J Optim Theory Appl 1985;45: 41–51.
41. Lin S, Kernighan BW. An effective heuristic algorithm for the traveling-salesman problem. Oper Res 1973;21:498–516.
42. Setsompop K, Gagoski BA, Polimeni JR, Witzel T, Wedeen VJ, Wald LL. Blipped-controlled aliasing in parallel imaging for simultaneous multislice echo planar imaging with reduced g-factor penalty. Magn Reson Med 2012;67:1210–1224.
43. Feinberg DA, Setsompop K. Ultra-fast MRI of the human brain with simultaneous multi-slice imaging. J Magn Reson 2013;229:90–100.
44. Moeller S, Yacoub E, Olman CA, et al. Multiband multislice GE-EPI at 7 tesla, with 16-fold acceleration using partial parallel imaging with application to high spatial and temporal whole-brain fMRI. Magn Reson Med 2010;63:1144–1153.
45. Barth M, Breuer F, Koopmans PJ, Norris DG, Poser BA. Simultaneous multislice (SMS) imaging techniques. Magn Reson Med 2016;75:63–81.
46. Deb K, Pratap A, Agarwal S, Meyarivan T. A fast and elitist multiobjective genetic algorithm: NSGA-II. IEEE Trans Evol Comput 2002;6: 182–197.
47. Knowles JD, Watson RA, Corne DW. Reducing local optima in single-objective problems by multi-objectivization. In Proceedings from the First International Conference on Evolutionary Multi-Criterion Optimization, Zurich, Switzerland, 2001. pp 269–283.
48. Santyr GE. Magnetization transfer effects in multislice MR imaging. Magn Reson Imaging 1993;11:521–532.
49. Shin K, Ahn K, Choi H, et al. DCE and DSC MR perfusion imaging in the differentiation of recurrent tumour from treatment-related changes in patients with glioma. Clin Radiol 2014;69:e264–e272.

SUPPORTING INFORMATION

Additional Supporting Information may be found in the online version of this article.

Fig. S1. Reconstructed T_1 maps for a representative slice for all measurements for the 100, 50, and 25 slices case.
Fig. S2. Reconstructed T_1 maps of 100 slices acquired with the optimized 4-measurement protocol.
Fig. S3. Reconstructed T_1 maps of 100 slices acquired with the optimized 5-measurement protocol.
Fig. S4. Reconstructed T_1 maps of 100 slices acquired with the optimized 8-measurement protocol.
Fig. S5. Reconstructed T_1 maps of 100 slices acquired with the optimized 10-measurement protocol.
Fig. S6. Reconstructed T_1 maps of 100 slices acquired with the optimized 16-measurement protocol.
Fig. S7. Reconstructed T_1 maps of 100 slices acquired with the unoptimized 21-measurement protocol.
Fig. S8. S_0 maps for the 8- and 21-measurement protocols. Note the similarity between the maps obtained with the two measurements.
Table S1. Summary of the TI values sampled as a function of the number of measurements for the 100-slice protocol
The range (max–min) of TI values was computed for each individual slice. The values reported here represent the mean and standard deviation of the range across all slices for each protocol.